Numerical Simulation of Unsteady Flow About Cambered Plates

Turgut Sarpkaya,* Samir M. Mostafa,† and Paul D. Munz‡
Naval Postgraduate School, Monterey, California

Reported herein is a theoretical and experimental investigation of a nonimpulsively-started steady ambient flow, subsequently decelerating to rest at prescribed rates, about two-dimensional cambered plates (circular arcs with included angles of 120, 180, and 240 deg) for the purpose of understanding the consequences of wake return and secondary separation on impermeable rigid surfaces. The numerical simulations are based on computational methods with vortices. Experiments are carried out in a vertical water tunnel. The results of the physical and numerical experiments are found to be in good agreement.

Nomenclature

A_p = $B_o\,dU/dt/U_o^2$, or $B_o^n\,d^nU/dt^n/U_o^{n+1}$, acceleration parameters
B_o = opening width of cambered plate, $= 2R\sin\alpha = 4b$
B_p = projected width of cambered plate
b = $B_o/4$
C_d = drag coefficient, $D/(2\rho bU_o^2)$
c = radius of the circular cylinder
D = drag force per unit length
i = imaginary number
K_{sbr} = B_p/W_t, solid blockage ratio
q = velocity vector
p = pressure
R = radius of the camber
$R\{\}$ = real part of a complex quantity
Re = Reynolds number, $= B_oU_o/\nu$
r = radial distance
T = U_ot/c, normalized time
T^* = time at onset of deceleration
t = time
U = velocity
$\dot{U}$ = dU/dt, acceleration
U_o = steady ambient velocity
U_s = velocity at separation point
u = x component of velocity
V_1 = tip velocity
V_2 = velocity at the inner edge of the shear layer
V_t = tangential velocity component
v = y component of velocity
W_t = tunnel width (24 in.)
w = complex potential function
z = $x + iy$, a point in the physical plane
z_n = location of the nth vortex
z_t = tip coordinate in the physical plane
Δt = time increment
Γ_n = circulation of the nth vortex
2α = included camber angle
ζ = $\xi + i\eta$, normalized location in circle plane
ζ_o = nascent vortex position in circle plane
ζ_t = position of camber edge in circle plane
ζ_v = position of a vortex in circle plane
θ = counter-clockwise angular position
θ_s = angular position of separation point
ν = kinematic viscosity
ρ = density of water

Introduction

THE genesis of the investigation is the determination of the deployment sequence of an axisymmetric porous parachute and the unsteady aerodynamic loads acting on it. The development of an analytical or numerical model that takes into account the effects of porosity, gaps, and variable opening schemes would allow numerical experiments on a large class of parachutes, reduce the number of expensive field tests to a few judiciously selected ones, and enable the designer to calculate the time history of the fall of the parachute and the strength required to survive the aerodynamic loads. However, the development of such a model is hampered by a number of difficulties, the most important being the lack of controlled laboratory experiments.

The previous models for parachute loads are based by and large on empirical assumptions.[1-3] The vortex-sheet analysis was used by Klimas[4] to derive the acceleration-independent apparent-mass coefficient for arbitrary-shaped axisymmetric surfaces. Muramoto and Garrard[5] used a continuous-source model to predict the steady-state drag of ribbon parachutes. Shirayama and Kuwahara[6] used a three-dimensional method with vortex sticks to simulate steady flow past a circular disk. None of these investigations dealt with the evolution of the wake during the period of rapid deceleration of the flow.

It is in view of the foregoing that a numerical and experimental study of the separated time-dependent flow about two-dimensional rigid cambered plates was undertaken. Clearly, such a flow is considerably simpler than that about a porous, axisymmetric, and flexible parachute, and the experimental data, regardless of the degree of their agreement with the corresponding analyses, may not have direct relevance to the practical problem under consideration. But the object of this investigation was the understanding of the evolution of the wake under controlled laboratory conditions rather than the development of a design tool. It is hoped that a study of this type will reveal the underlying physics of the phenomenon (particularly that of the parachute collapse), help to interpret the full-scale results and provide inspiration for the development of suitable numerical models with which the dynamics of axisymmetric, porous, and flexible parachute canopies can be investigated.

The existing finite difference methods cannot yet treat the high Reynolds number flows with sufficient accuracy for a

Received Oct. 29, 1988; presented as Paper 89-0290 at the AIAA 27th Aerospace Sciences Meeting, Reno, NV, Jan. 9-12, 1989; revision received June 22, 1989.

*Distinguished Professor of Mechanical Engineering. Associate Fellow AIAA.
†Colonel, Egyptian Air Force.
‡Lieutenant Commander, U.S. Navy.

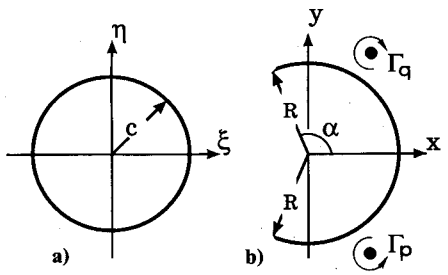

Fig. 1 a) Circle plane, b) Physical plane.

number of reasons. They require a very fine grid, a turbulence model, and a very large computer. It seems that the modeling of the turbulent stresses in the wake, particularly in time-dependent flows, will be the major source of difficulty in all future calculations. The inherent difficulties are certainly significant enough to warrant exploring other solution methods.

Certain separated time-dependent flows may be simulated through the use of the discrete vortex model (DVM).[7] The free shear layers which emanate from the sides of the body are represented by an assembly of discrete vortices. The strength of the elemental vortices are determined through the use of the Kutta condition. The use of a suitable convection scheme enables one to march in time and to calculate the evolution of the wake, the velocity and pressure distributions, and the lift and drag forces acting on the body. The numerical work described herein deals with the application of the DVM to flow decelerating to rest from an impulsively started steady ambient flow about two-dimensional cambered plates.

Analysis

Conformal Transformations and Velocity Potential

The calculation of the velocity of any one of the vortices and the force acting on the body requires a conformal transformation (in which the camber becomes a circle), a complex-velocity potential representing the vortices, their images, and the two-dimensional irrotational flow around the body, and the use of the generalized Blasius theorem.

The flow in the circle plane (Fig. 1a) may be transformed to that about a cambered plate (Fig. 1b) through the use of

$$z = \zeta + m - \frac{b^2}{\zeta + m} + \frac{1 - 2m^2}{m} \tag{1}$$

Table 1 summarizes the relationships between m, α, b, and the radius of the camber.

The complex velocity potential w in the circle plane, which describes a uniform flow U (assumed to be time dependent) with a doublet at the origin to simulate the cylinder, Γ_{kq} clockwise-rotating vortices (called q vortices), Γ_{kp} counterclockwise-rotating vortices (called p vortices), and the images of all the p and q vortices in the circle plane, may be written as

$$\begin{aligned} w = &-U\left(\zeta + \frac{c^2}{\zeta}\right) + \frac{i\Gamma_{op}}{2\pi} Ln(\zeta - \zeta_{op}) - \frac{i\Gamma_{op}}{2\pi} Ln\left(\zeta - \frac{c^2}{\bar{\zeta}_{op}}\right) \\ &+ \sum \frac{i\Gamma_{kp}}{2\pi} Ln(\zeta - \zeta_{kp}) - \sum \frac{i\Gamma_{kp}}{2\pi} Ln\left(\zeta - \frac{c^2}{\bar{\zeta}_{kp}}\right) \\ &- \frac{i\Gamma_{oq}}{2\pi} Ln(\zeta - \zeta_{oq}) + \frac{i\Gamma_{oq}}{2\pi} Ln\left(\zeta - \frac{c^2}{\bar{\zeta}_{oq}}\right) \\ &- \sum \frac{i\Gamma_{kq}}{2\pi} Ln(\zeta - \zeta_{kq}) + \sum \frac{i\Gamma_{kq}}{2\pi} Ln\left(\zeta - \frac{c^2}{\bar{\zeta}_{kq}}\right) \end{aligned} \tag{2}$$

in which Γ_{kp} and ζ_{kp} represent, respectively, the strength and location of the kth p vortex, Γ_{kq} and ζ_{kq} the strength and location of the kth q vortex, and c the radius of the cylinder; an overbar indicates a complex conjugate. The need for the separate identification of the p and q vortices and for the singling out of the nascent vortices in each shear layer (i.e., Γ_{op} and Γ_{oq}) will become clear later.[8,9]

Table 1 Geometrical relationships

	m/c	2α	b/c	$R/c = 1/m$
Model A	0.500	120	0.866	2
Model B	0.707	180	0.707	$\sqrt{2}$
Model C	0.866	240	0.500	$2/\sqrt{3}$

Complex Velocities of Vortices

The convection of the vortices and the calculation of the forces acting on the body require the evaluation of the velocities at the vortex centers in the physical plane. Using Routh's rule,[7-10] one has

$$-u_x + iv_y = \frac{d}{d\zeta}\left[w(\zeta) - \frac{i\Gamma}{2\pi} Ln(\zeta - \zeta_v)\right]\frac{1}{f'(\zeta)}\Bigg|_{\zeta=\zeta_v} - \frac{i\Gamma}{4\pi}\frac{f''(\zeta_v)}{f'^2(\zeta_v)} \tag{3}$$

in which the last term in Eq. (3), for a p vortex, for example, reduces to

$$\frac{i\Gamma_{kp}}{4\pi}\frac{b^2(\zeta_{kp} + m)}{[(\zeta_{kp} + m)^2 + b^2]^2} \tag{4}$$

Similar results may be obtained for other vortices.

The fact that the flow separates tangentially with a finite velocity at the edges of the camber (Kutta condition) may be expressed by requiring

$$dw/d\zeta = 0 \quad \text{at} \quad \zeta = \zeta_t = -m \pm ib \tag{5}$$

Thus, inserting Eq. (2) in Eq. (5), one has

$$\begin{aligned} &\frac{i\Gamma_{op}}{2\pi}\left(\frac{1}{\zeta_t - \zeta_{op}} - \frac{1}{\zeta_t - \frac{c^2}{\bar{\zeta}_{op}}}\right) - \frac{i\Gamma_{oq}}{2\pi}\frac{1}{\zeta_t - \zeta_{oq}} - \frac{1}{\zeta_t - \frac{c^2}{\bar{\zeta}_{oq}}} \\ &+ \sum \frac{i\Gamma_{kp}}{2\pi}\left(\frac{1}{\zeta_t - \zeta_{kp}} - \frac{1}{\zeta_t - \frac{c^2}{\bar{\zeta}_{kp}}}\right) \\ &- \sum \frac{i\Gamma_{kq}}{2\pi}\left(\frac{1}{\zeta_t - \zeta_{kq}} - \frac{1}{\zeta_t - \frac{c^2}{\bar{\zeta}_{kq}}}\right) - U\left(1 - \frac{c^2}{\zeta_t^2}\right) = 0 \end{aligned} \tag{6}$$

Equation (6) may be decomposed into two parts as

$$\begin{aligned} &\frac{i\Gamma_{op}}{2\pi}\left(\frac{1}{\zeta_t - \zeta_{op}} - \frac{1}{\zeta_t - \frac{c^2}{\bar{\zeta}_{op}}}\right) \\ &- \frac{i\Gamma_{oq}}{2\pi}\left(\frac{1}{\zeta_t - \zeta_{oq}} - \frac{1}{\zeta_t - \frac{c^2}{\bar{\zeta}_{oq}}}\right) - u_o + iv_o = 0 \end{aligned} \tag{7}$$

where the terms containing the strength of the nascent vortices represent the velocity induced at the tip of the camber by the nascent vortices and $(-u_o + iv_o)$, the velocity at the tip due to all other vortices (and their images), the doublet at the center of the circle in the ζ plane, and the ambient velocity.

Equation (7) represents two coupled equations for the strengths and positions of the nascent vortices. Thus, the solution of the said equations does, in general, require an iteration. However, this iteration may be avoided by noting that the velocity induced by a nascent vortex at the opposite tip is very small and certainly negligible. Thus, Eq. (7), for one of the nascent vortices, may be reduced to

$$-\frac{i\Gamma_{oq}}{2\pi}\left(\frac{1}{\zeta_t - \zeta_{oq}} - \frac{1}{\zeta_t - \dfrac{c^2}{\bar{\zeta}_{oq}}}\right) - u_o + iv_o = 0 \qquad (8)$$

A similar expression may be written for the other nascent vortex.

Computational Details

First, the velocities V_1 (tip velocity) and V_2 (velocity at the downstream face of the camber near the tip) are calculated. The tip velocity is exactly given by[9]

$$\left.\frac{dw}{dz}\right|_{z=z_t} = \frac{d^2w}{d\zeta^2}\frac{ib}{2} \qquad (9)$$

The velocity V_2 at the inner edge of the shear layer is, in general, small, except near the end of the deceleration period during which the wake return is prominent and the large scale structures give rise to secondary separations on the rear face of the camber. Obviously, the 'inner edge' is dictated by the sign of the nascent vortex. For a clockwise nascent vortex (see Γ_q in Fig. 1b), the inner edge is the downstream side of the tip. For a counterclockwise nascent vortex, the inner edge is the upstream side of the tip.

The nascent vortex strength, the velocities on either side of the shear layer, and the time interval are related by

$$\Gamma = 0.5\,(V_1^2 - V_2^2)\Delta t \qquad (10)$$

Numerous approximate schemes have been devised in the past to introduce the nascent vortices. (A detailed discussion of these is presented by Sarpkaya.[7]) The most common among these is the use of fixed points, a short distance ϵ downstream of the separation points, in the planes of the body sides. The range of the disposable parameter ϵ was determined by trial computations, using the stability of the Strouhal number and the form of the vortex cluster as criteria. Giesing[11] has shown that the flow must leave the edge tangentially to the windward side, provided that the sheet is modeled by a *continuous sheet of vorticity* in the vicinity of the edge. However, when discrete vortices are used to introduce vorticity, the correct position of the nascent vortex does not necessarily lie on the tangent. This is particularly true for bodies with upstream-facing sharp-edges (e.g., a parachute canopy), where the radius of curvature of the vortex sheet is very small near the edge. Only the unique positions of the nascent vortex yield separation-velocity profiles that are compatible with the condition that in an inviscid flow the velocity and acceleration extrema occur on the body.[10] The time step, the separation point velocity, and the point of nascent vortex introduction are interrelated and none can be assigned arbitrarily or on the basis of trial calculations.

It is on the basis of the foregoing that the calculations are carried out as follows:

1) Select an initial vortex position along a radial line from the tip. It is only unique combinations of the radial distance and the angular position of the nascent vortex (relative to the tangent at the tip) that the tip velocity V_1 is the maximum of the velocities in the vicinity of the tip. The direction of the radial line, for which the velocity maximum occurs on the body, is determined by iteration. The details of this relatively simple and unambiguous procedure are described by Sarpkaya et al.,[9] Mostafa,[10] and Munz.[12]

2) Calculate the strength of the nascent vortex from Eq. (8), or from its equivalent for the other nascent vortex, which satisfies the Kutta condition for a prescribed ambient flow condition. This is an exact solution and requires no iteration.

3) Place the nascent vortex at the corresponding points in the circle and physical planes and calculate the tip velocity.

4) Calculate a new nascent vortex strength from Eq. (10) and compare the newly calculated circulation with that obtained from the Kutta condition. If the difference between the two circulations is less than a prescribed error $\Delta\gamma$ (0.001), proceed to the next step. If the said difference is larger than $\Delta\gamma$, carry out an iteration on the radial location of the nascent vortex as many times as necessary until the above condition is satisfied. If the circulation calculated from the Kutta condition is larger than that calculated from the tip velocities, the vortex must be moved toward the cylinder and vice versa. Also, each time the direction of the motion of the nascent vortex changes (inward or outward), the marching distance is halved in order to accelerate the convergence of the two calculations. The above procedure establishes, for the first time, a unique relationship between the nascent-vortex strength, nascent-vortex position, and the time interval. As noted above, in all previous studies, the time interval and/or the vortex position was chosen on the basis of ad hoc assumptions or on the basis of previous experience or trial calculations.

5) Calculate the velocity induced at the center of all vortices and the velocity distribution in the vicinity of the tips.

6) Convect the nascent vortices with a velocity $(V_1 + V_2)/2$ for a time interval Δt.

7) Convect all other vortices for the same time interval, using a second-order Eulerian scheme.

8) Calculate the tangential velocities and pressures on the inner and outer faces of the camber. The differential pressure between two points m and n is given by

$$\frac{p_m - p_n}{\rho U_o^2/2} = \frac{V_1^2 - V_2^2}{U_o^2} + \frac{V_n^2 - V_m^2}{U_o^2} + \frac{\partial}{\partial t}\int_m^n 2\frac{V_t}{U_o^2}\,ds \qquad (11)$$

The integration of the differential pressure between the upstream and downstream faces of the camber yields the force components in the x and y directions, i.e., the drag- and lift-force coefficients.

9) Update the ambient flow conditions and make the desired plots and return to step 1.

The foregoing calculations were also done using variable time steps and fixing the position of the nascent vortices along the radial lines (see step 1). The details are described in Sarpkaya et al.[9] A particular run required about 150 vortices on each side of the camber. Extensive experience with the two versions of the code has shown that a run takes about three hours on an IBM PC/AT. Furthermore, the constant-time-interval version of the program ran slightly faster than the variable-time-interval version, in spite of the iterations required for the nascent vortex position. Suffice it to note that both versions of the code yielded almost exactly identical results for a given camber and velocity history.

Experiments

The experiments were conducted in a 17 ft (5.2 m) high, 2 ft × 2 ft (0.61 m × 0.61 m) cross-sectional vertical water tunnel.[9,13] A quick-release valve located at the base of the tunnel is used to create an almost impulsively-started flow of desired velocity history (except at the initial instants of about 0.3 s or so).

Experiments were first carried out with three circular arcs[9] (fabricated from aluminum pipes with a wall thickness of 1/16 in.) of radius 1.5 in. (38.1 mm), length 24.5 in. (62.2 cm), and included angles of 120 deg (model A), 180 deg (model B), and

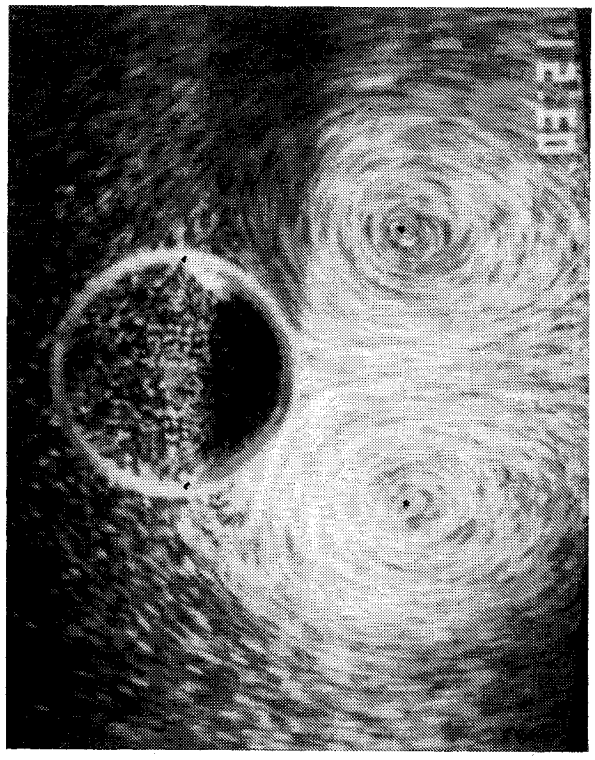

Fig. 2 Sample flow visualization with polystyrene beads about a 180-deg cambered plate.

240 deg (model C). The solid blockage ratio $K_{sbr}(=B_p/W_t)$ was 1/9.23 for model A, and 1/8 for models B and C. Then the experiments were repeated with three similar circular arcs of radius 1.0 in. (25.4 mm). For this set, K_{sbr} was 1/13.84, 1/12, and 1/12 for models A, B, and C, respectively.

The edges of the cambered plates were first cut razor sharp (machining only the outer faces of the edges and maintaining the inside radius) and then gently rounded with sand paper. Each end of a model was terminated with a 0.25 in. (6.4 mm) long circular section (part of the original pipe from which the model was cut out). These end sections served several purposes. First, they prevented the distortion of the prestressed cambered plates. Second, they provided a clear view of the flow for visualization when imbedded rigidly in a plexiglass window (this circle shows in the photographs: see, e.g., Fig. 2). Third, they enabled the measurement of the drag force when fitted with circular metal disks and extension rods, going through the holes in the plexiglass windows. There was a gap of approximately 0.04 in. (1 mm) between the hole and the end section. The flow sides of the metal or plexiglass disks at the ends of the camber were flush with the tunnel walls, i.e., there was no obstruction to the flow before it reached the cambered plate. The extension rods at both ends of the model were inserted into the self-aligning ball bearings of the strain-gauged load cells (Baldwin-Lima-Hamilton LBP gauges), mounted on the tunnel windows. The gauges had ample dynamic response for the measurements reported herein.

The ambient velocity was determined from the integration of the instantaneous acceleration. Prior to conducting any experiments, impulsive flow was initiated several times to check the operation of the system. Adjustments to the control system of the quick-release-valve were made, as necessary, to ensure the repeatability of the desired variation in velocity and acceleration.

The variations of velocity and acceleration with time were either represented by suitable functions or left in digitized form for use in the numerical calculations. A sample velocity history (see Fig. 3) is given by

$$U/U_o = 1 \quad \text{for} \quad T = 10.2 \tag{12a}$$

$$U/U_o = 0.5 + 0.5\cos[0.5233\,(T - 10.2)] \text{ for } 10.2 < T < 16.28 \tag{12b}$$

Clearly, Eq. (12a) assumes that the flow is accelerated impulsively from rest to a constant velocity. In general, this is not possible, as seen in Fig. 3, and the measured and calculated forces differ at small times because of the difference between the measured and assumed initial acceleration histories. Suffice it to note that, other than numerical experiments, there is no mechanical or traveling-shock system that is capable of generating a truly impulsive flow. Efforts to generate impulsive or uniformly-accelerated flow at high Reynolds numbers or accelerations in a liquid medium are hampered by the generation of compression and rarefaction waves and regions of intense cavitation. These are some of the difficulties of the experiments with impulsive flows.

Impulsively-started steady flow is a very special case of unsteady flows starting from rest and reaching a steady state over a time period. In general, the rate of accumulation of vorticity, onset of wake asymmetry, and the evolution of the in-line and transverse forces are dependent on the parameters characterizing the *nonimpulsive* nature of the ambient flow,[14] (e.g., the acceleration parameter $A_p = B_o \cdot dU/dt/U_o^2$, in addition to the normalized time $T = U_o t/c$, the Reynolds number $U_o B_o/\nu$, and the higher order acceleration parameters, such as $B_o^n d^n U/dt^n/U_0^{n+1}$). All numerical calculations using finite-difference, finite-element, or discrete-vortex methods[7] have assumed an *impulsively* started flow. So far, no computational attempt has been made to investigate the effect of the initial acceleration, prior to the establishment of the steady uniform flow, on the characteristics of the resulting time-dependent flow. A systematic variation of A_p is extremely difficult. The best one can hope for is to maintain it as constant and as large as possible. For the data reported herein, A_p was about 1.2. Repeated experiments with smaller values of A_p have shown that the effect of the duration of the initial acceleration on the subsequent evolution of the flow is confined to a time period $(0 < T < 4)$, approximately 1.5 times the acceleration period (the first 0.45 s in Fig. 3).

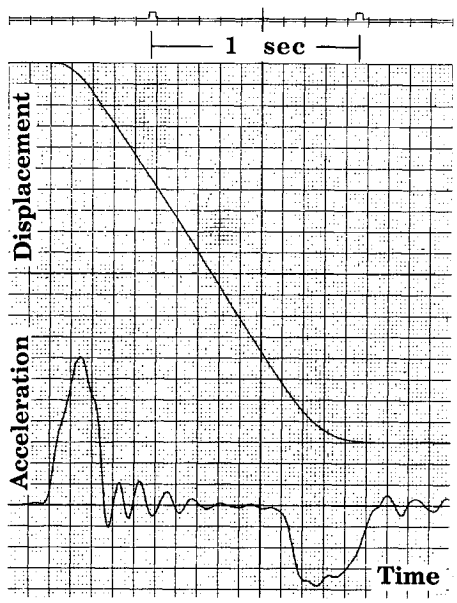

Fig. 3 Sample displacement and acceleration traces.

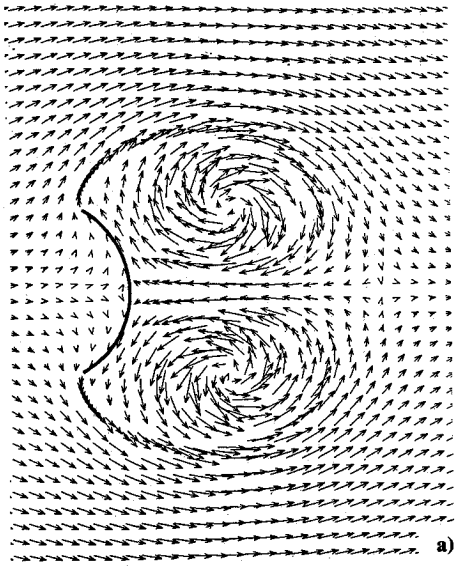

Fig. 4a Flow about a 120-deg cambered plate at $T = 8.55$.

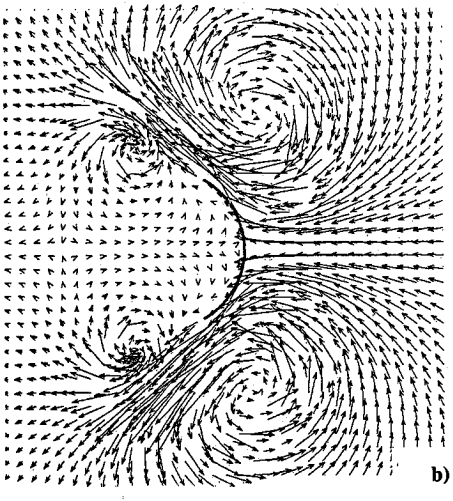

Fig. 4b Flow about a 120-deg cambered plate at $T = 18.35$.

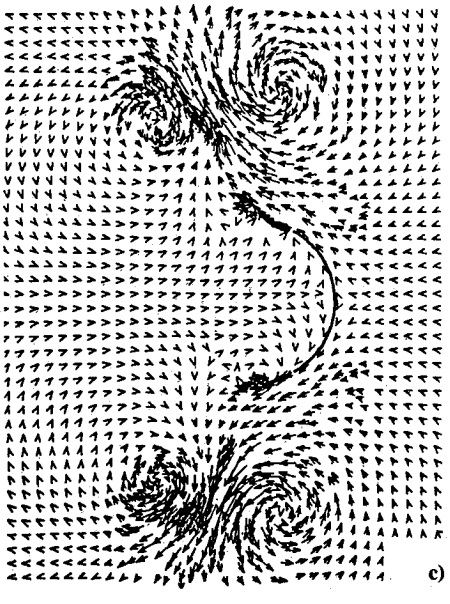

Fig. 4c Flow about a 120-deg cambered plate at $T = 21.50$.

Discussion of Results

Simulation of Separation at Camber Edges Only

Figures 4a–c, 5, and 6 show, at arbitrary times, the evolution of flow about the models A, B, and C. In general, two *nearly symmetric,* large-scale vortices develop during the short period ($T^* \approx 10$) of steady ambient flow. As the flow decelerates, these vortices move backwards and give rise to oppositely signed vorticity. This, in turn, leads to the rapid growth of two new vortices near the tips, as seen in Figs. 4b, 4c, 5b, and 6b.

Figures 7–9 show the comparison of the calculated and measured drag coefficients for the three models. The former is based on the integration of the differential pressure across the camber and the use of suitable functional relationships for the velocity and acceleration. The agreement between the measured and calculated values for the models A and B is quite encouraging. There are, however, some differences. The experimental values of C_d are somewhat larger than those calculated for T smaller than about 4 because of the fact that the calculations were based on an impulsively started uniform flow, prior to the onset of deceleration, whereas the experiments involved a relatively more complex flow establishment regime in the interval ($0 < T < 2.7$) (see the first 0.3 s in Fig. 3). Numerous experiments[9] with different steady-flow periods ($6 < T^* < 30$), prior to deceleration, have shown that the flow remains nearly symmetrical (with two growing vortices) for T^* less than about 30 ($U_o t/B_p \approx 8.7$) for model A, for T^* less than about 20 ($U_o t/B_p \approx 7$) for model B, and for T^* less than about 16 ($U_o t/B_p \approx 5.7$) for model C. In the case of a circular cylinder,[13] the first vortex is shed at $U_o t/D \approx 4.5$. It is noted that a circular cylinder has mobile separation points, whereas the cambered plates have fixed separation points.

The present investigation does not deal with flows decelerating from a state of *asymmetric* wake (i.e., T^* is kept smaller than about 11). Even then, the characteristics of flow after the onset of deceleration depend on the particular state of the symmetric wake from which the flow is decelerated, i.e., on T^*, in addition to the other parameters characterizing the

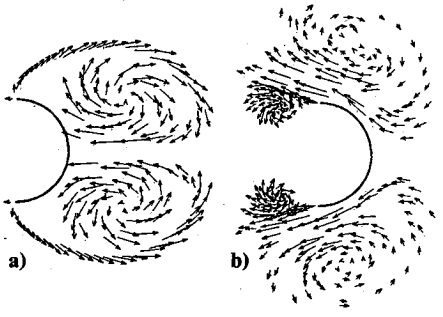

Fig. 5 Flow about a 180-deg cambered plate: a) $T = 10.35$, b) $T = 17.25$.

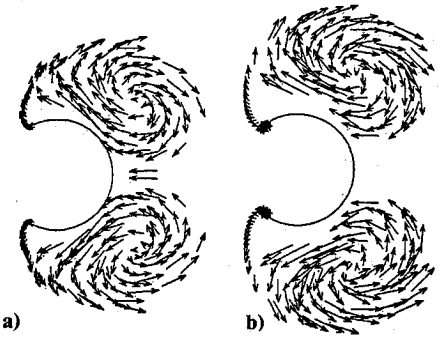

Fig. 6 Flow about a 240-deg cambered plate: a) $T = 13.25$, b) $T = 16.75$.

flow. Evidently, there are a wide class of unsteady flow problems concerning the response of the wake (transient or quasiperiodic) to nonimpulsively accelerated and/or nonimpulsively decelerated flow about bluff bodies. The present work deals only with a special class of these flows: deceleration from a particular state with a nearly symmetric wake. For sufficiently large T^*, the wake symmetry is destroyed by the presence of multiple and nondeterministic perturbation sources. When the flow is in a 'critical' state to become asymmetrical, a very small cause can have a very great effect. In numerical experiments, the perturbations of nature yielding the final asymmetry cannot be modeled with or without artificial perturbation sources.

The measured and calculated forces also differ toward the ends of the deceleration period for a number of reasons. This period of flow, where the ambient flow is nearly zero, is often accompanied by three-dimensional instabilities, secondary separation, generation of oppositely signed vorticity (on the back face of the camber) because of the return of the wake to the body, and turbulent diffusion of vortices. Thus, the relatively small drag forces occurring toward the end of the deceleration period are an integrated average of the effects of this three dimensionality, turbulent diffusion, and secondary separation on the pressure distribution. The fact that the differences between the measured and calculated drag forces are not attributable to the blockage effects is evidenced by the fact that the drag coefficients for the smaller and larger versions of models A, B, and C were found to be within the measurement uncertainty for the entire range of T. The secondary separations will be discussed in more detail later.

Figure 9 shows a comparison of the calculated and measured drag coefficients for model C. The agreement between the two C_d values is not satisfactory, even during the period prior to the onset of deceleration. The fundamental reason for this disagreement is that not enough physics has been built into the numerical model to deal with either the boundary-layer development during the early stages of the motion or with the rear-face separation during the later stages of the motion. Unlike the previous cases, the initial rise in the measured drag is followed first by a sharp decrease and then by a rise to a larger maximum. Subsequently, C_d decreases rapidly at the onset of deceleration, goes through zero near the middle of the deceleration period, and then through a relatively small minimum (negative) value at the end of the deceleration period. Subsequently, C_d gradually decreases to zero.

Extensive flow visualization experiments[9] with dyes and polystyrene beads have shown that the flow does not separate immediately at the sharp edges of model C, as in the cases of models A and B. The separation begins at the rear stagnation point and leads to the formation and growth of two small vortices (as if the camber were a circular cylinder immersed in an impulsively started flow). Subsequently, these vortices move toward the rear of the camber (the time at which the drag decreases sharply) and the separation points move rapidly to the edges of the camber. There is a time period during which there are four vortices in the wake (the two small vortices and the two larger ones, resulting from the separation at the sharp edges, see Fig. 10). Subsequently, the smaller vortices are overtaken by or merge with the larger ones. This merging takes place in a very short time (in about 0.03 s). The remaining vortices grow rapidly, move back towards the camber during deceleration, and give rise to two relatively large regions of the secondary separation near the rear edges of the camber. Subsequently, the vortex pairs of opposite sign, near each tip, propel each other upstream and sideways. It is important to note that separation during the period of deceleration occurs not only at the sharp edges but also at the downstream face of the camber (at about 30 deg downstream from the edges) partly due to the presence of the large afterbody (240-deg arc) and partly due to the large velocities induced on it. (For detailed flow visualization photographs see Sarpkaya et al.[9])

The foregoing explains in part the reason for the differences between the measured and calculated forces even during the early stages of the motion. The disagreement during the later stages of the motion is partly due to the development of strong three-dimensional instabilities in vortices during the deceleration period, partly due to the occurrence of rear-face separation, and partly due to the fact that the numerical model does not account for the turbulent diffusion of vortices. As noted earlier, the effect of the secondary separation becomes progressively more pronounced as the included angle of camber

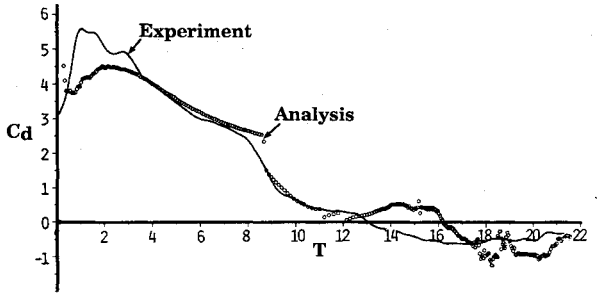

Fig. 7 Comparison of measured and predicted drag coefficients for model A (tip separation only).

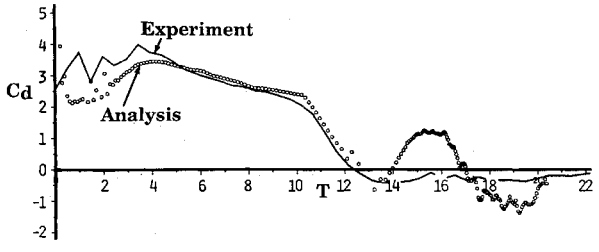

Fig. 8 Comparison of measured and predicted drag coefficients for model B (tip separation only).

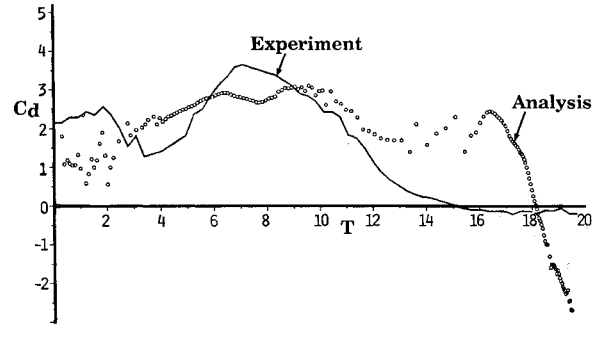

Fig. 9 Comparison of measured and predicted drag coefficients for model C (tip separation only).

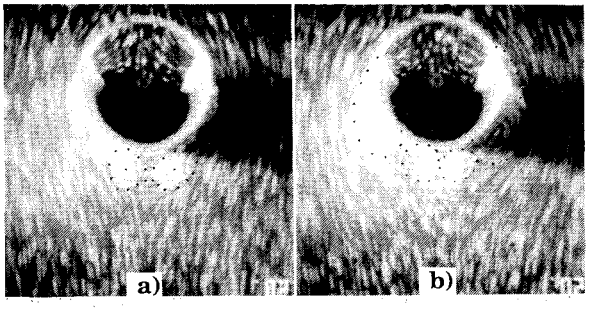

Fig. 10 Initial instants of flow separation about model C: a) two vortices, b) four vortices.

increases. This is true for all bluff-body problems where the afterbody (the part of the body beyond the mobile or fixed primary separation points) is large. In this sense, the model C becomes one of the most challenging bluff-body shapes as far as the computational methods with vortices are concerned. The problem is further compounded by the fact that the ambient flow is not steady and the vortices return to the body during the period of deceleration. In fact, the understanding of the attendant consequences of this wake return in experiments and numerical analysis constitutes the essence of the investigation. Sufficient physics will have to be incorporated into the numerical model to deal with these complex problems without resorting to the use of ad hoc assumptions, such as artificial reduction of circulation.

Simulation of Separation at Edges and Rear

The foregoing discussion pointed out the need for the inclusion into the numerical analysis of at least the oppositely signed vorticity, generated on the downstream face of the camber. The turbulent diffusion can neither be modeled with vortex methods nor be distinguished from numerical diffusion.

The inclusion of oppositely signed vorticity is accomplished, as follows:

1) Tangential velocity distribution on the downstream face of the camber is calculated.

2) The camber is divided into $\Delta\theta$-deg angular intervals ($\Delta\theta = 3$ deg for model A, $\Delta\theta = 4.5$ deg for model B, and $\Delta\theta = 6$ deg for model C, i.e., 40 nascent vortices are used for each model to represent the secondary vorticity generation).

3) The strength of each nascent vortex is calculated from $\Delta\Gamma_i = q_i(\theta) \cdot R \cdot \Delta\theta$ (where $R \cdot \Delta\theta = \Delta s$, the elemental arc length).

4) The nascent vortices are placed on radial lines, bisecting the segments, at a radial distance so as to satisfy the no-slip condition (a simulation of the vorticity generation in real fluids).

5) The velocity at the position of each vortex is calculated through the use of the Biot-Savart law and the vortices are convected for a small time interval Δt. The vortices which move into the body are reflected back. The nascent vortices emanating from the tips of the camber are treated in exactly the same manner as described previously.

Conceptually, there is no difficulty in devising the above model since it does not require any ad hoc assumptions. However, there is one fundamental difficulty that permeates the application of all discrete vortex models, i.e., the CPU time. This is evidenced by the fact that 42 new vortices are shed at each time step (40 vortices from the back face and 2 from the tips of the camber). Thus, at time $T = 20$ (the approximate end of the computation), the flowfield acquires 8400 vortices. Since the Biot-Savart law requires N^2 calculations at each time step (N being the number of vortices), the CPU time increases dramatically relative to the case of tip-separation only. Aside from this obvious drawback, there are no difficulties associated with the calculations.

Figures 11–13 show sample plots of the flow about the three models. Figures 14–16 show the measured and predicted force-time histories. It is clear from these figures that there is good to excellent agreement between the measurements and predictions throughout the duration of the runs. For very small times (T less than about 4, corresponding to about 0.45 s in real time), the measured and calculated forces differ, as previously noted. This is not due to a shortcoming of the analysis but rather due to the fact that in the calculations the flow was started impulsively from rest with a uniform velocity. In the experiments, such an impulsive start is impossible and the early acceleration history shows its effect on the measured force. Once the acceleration history disappears and the ambient flow becomes steady, the measured and calculated forces match reasonably well. It was, of course, possible to input into

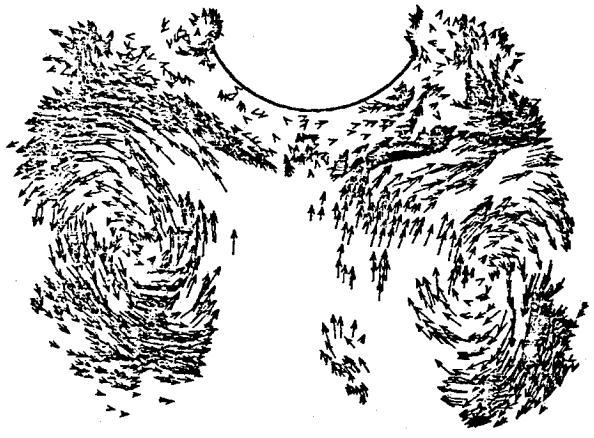

Fig. 11 Flow about model A with rear separation ($T = 16.75$).

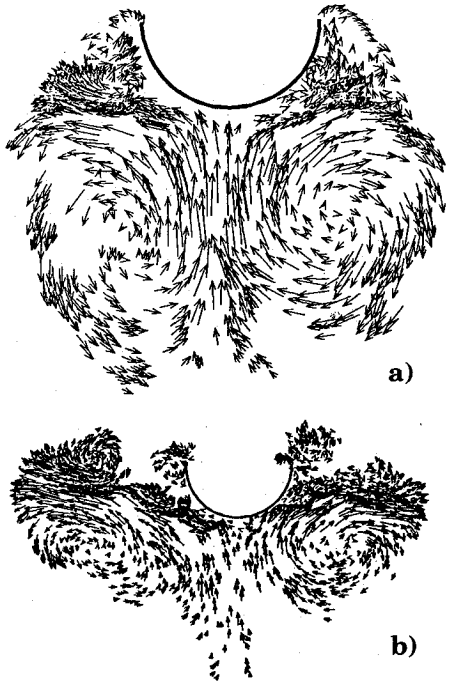

Fig. 12 Flow about model B with rear separation a) $T = 13.85$, b) $T = 17.25$.

Fig. 13 Flow about model C with rear separation ($T = 14.50$).

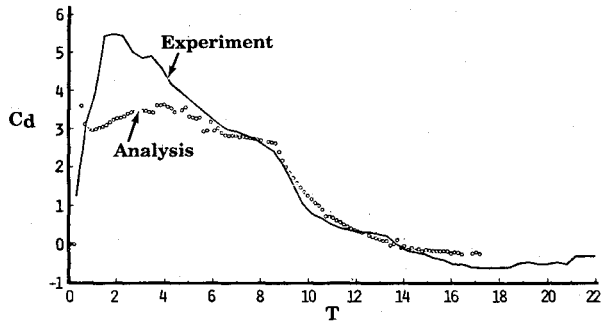

Fig. 14 Comparison of measured and predicted drag coefficients for model A (with rear separation).

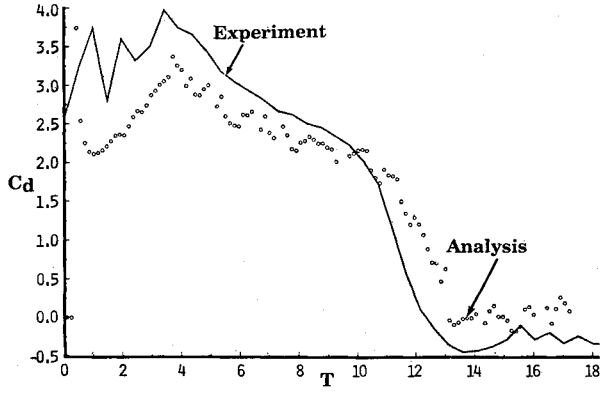

Fig. 15 Comparison of measured and predicted drag coefficients for model B (with rear separation).

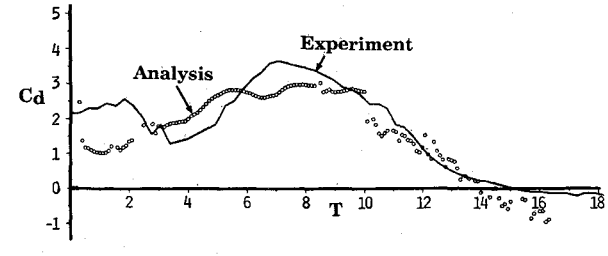

Fig. 16 Comparison of measured and predicted drag coefficients for model C (with rear separation).

the calculations the measured velocity and acceleration history at the start of the calculations and, thereby, obtain a better agreement between the various measured and predicted C_d in the early stages of the motion. This was deemed unnecessary due to the previously noted fact that the force becomes independent of the acceleration history shortly after the ambient velocity reaches a constant value, at least for the flow under consideration.

Figures 14–16 show that the calculated force deviates from that measured for T larger than about 13. This is toward the end of the deceleration period and involves very little forces. In any case, one should bear in mind that the shape of the model C is more conducive to turbulent diffusion of vortices and to three-dimensional flow effects relative to models B and C. Such effects could partially account for the small differences between the two negligibly small (measured and calculated) forces.

Conclusions

A numerical and experimental investigation of a nonimpulsively started uniform flow, decelerating at prescribed rates, about two-dimensional cambered plates with included angles of 120, 180, and 240 deg has been carried out.[9] The results have shown the following:

1) For models A and B, the flow separates at the sharp edges right from the start and remains there throughout the rest of the motion. Two nearly symmetrical primary vortices form and continue to grow during the periods of initial acceleration and subsequent steady flow. The regions of secondary flow near the rear edges of the camber are quite small. During the period of deceleration, the vortices move toward the camber, develop three-dimensional instabilities, and give rise to oppositely signed circulation at the inner edges of the camber. Subsequently, the vortices continue to move sideways and the forces acting on the camber reduces to zero as the vortices are diffused by both molecular and turbulent diffusion.

2) For model C (240-deg camber), the initial rise in C_d is followed by a sharp decrease and then by a rise to a larger maximum. Subsequently, C_d decreases rapidly at the onset of deceleration, goes through zero near the middle of the deceleration period, and through a relatively small (negative) minimum value at the end of the deceleration period. The flow does not separate immediately at the sharp edges of the camber. The separation begins at the rear stagnation point and leads to the formation and growth of two small vortices. Subsequently, these vortices merge with the primary vortices emanating from the tips.

3) The use of a multivortex separation model accounts for the evolution of the tip vortices and with the generation of oppositely signed vorticity on the downstream face of the camber. This model leads to results that agree rather satisfactorily with those obtained experimentally. This is as good as one could ever expect from the computational methods with vortices without the use of ad hoc assumptions, such as the artificial reduction of circulation. The remaining small differences between the measurements and predictions may be attributed to the three-dimensional wandering of the vortex axis and turbulent diffusion of vortices, particularly for models with large angles of camber.

4) The calculations show[9] that following the onset of deceleration and wake return, the differential pressure near the axis of the camber becomes increasingly negative. Had the model been flexible (as in the case of a parachute), the central part of the camber would have collapsed as a result of the particular deceleration it is subjected to. Evidently, the parachute collapse phenomenon would not have remained symmetrical, as evidenced by field experiments[15] with large axisymmetric parachutes.

5) Fast numerical experiments can be carried out with the model developed herein. It would have been extremely difficult, if not impossible, to achieve similar results with space-discretization methods, within comparable CPU times. Thus, the investigation reported herein shows the power as well as the limitations of the computational methods with vortices through the use of three highly complex separated time-dependent flows. The results are in conformity with the more modest objectives of vortex models: identification of large-scale structures rising above (or floating over) the small-scale turbulence and acquisition of new insights. The mismatch between model-based predictions and experimental results is not entirely due, or always attributable, to deficiencies in the model, but also lies in the three-dimensional nature of 'two-dimensional' experiments.

Acknowledgments

The investigation has been supported by the Sandia National Laboratories. A special note of thanks is extended to Jack McKay for his most skillful and dedicated work in the construction and operation of the test facilities.

References

[1]Heinrich, H. G. and Saari, D. P., "Parachute Opening Shock Calculations with Experimentally Established Input Functions," *Journal of Aircraft,* Vol. 15, No. 2, Feb. 1978, pp. 100–105.

[2]McVey, D. F. and Wolf, D. F., "Analysis of Deployment and Inflation of Large Ribbon Parachutes," *Journal of Aircraft,* Vol. 11, Feb. 1972, pp. 96–103.

[3]Cockrell, D. J., "The Aerodynamics of Parachutes," AGARD-AG-295, 1987.

[4]Klimas, P. C., "Fluid Mass Associated with an Axisymmetric Parachute Canopy," *Journal of Aircraft,* Vol. 14, No. 6, June 1977, pp. 577–580.

[5]Muramoto, K. K. and Garrard, W. L., "A Method for Calculating the Pressure Filed about a Ribbon Parachute Canopy in Steady Descent," AIAA-84-0794, 1984.

[6]Shirayama, S. and Kuwahara, K., "Computation of Flow Past a Parachute by a Three-Dimensional Vortex Method," AIAA-86-0350, 1986.

[7]Sarpkaya, T., "Computational Methods with Vortices—The 1988 Freeman Scholar Lecture," *Journal of Fluids Engineering, Trans. ASME,* Vol. 111, No. 1, March 1989, pp. 5–52.

[8]Sarpkaya, T., "An Inviscid Model of Two-Dimensional Vortex Shedding for Transient and Asymptotically Steady Separated Flow Over an Inclined Flat Plate," *Journal of Fluid Mechanics,* Vol. 68, March 1975, pp. 109–128.

[9]Sarpkaya, T., Mostafa, S. I. M., and Munz, P. D., "Unsteady Flow about Cambered Plates," Naval Postgraduate School, Monterey, CA, TR NPS-69-87-012, Oct. 1987.

[10]Mostafa, S. I. M., "Numerical Simulation of Unsteady Separated Flows," Ph.D. Thesis, Naval Postgraduate School, Monterey, CA, 1987.

[11]Giesing, J.P., "Vorticity and Kutta Condition for Unsteady Multienergy Flows," *Journal of Applied Mechanics,* Vol. 36, Sept. 1969, pp. 608–613.

[12]Munz, P. M., "Unsteady Flow about Cambered Plates," M.S. Thesis, Naval Postgraduate School, Monterey, CA, 1987.

[13]Sarpkaya, T., "Impulsive Flow About a Circular Cylinder," Naval Postgraduate School, Monterey, CA, TR NPS-69SL-78-008, March 1978.

[14]Sarpkaya, T., "Non-impulsively-started Steady Flow About a Circular Cylinder," AIAA Paper 90-0578, Jan. 1990).

[15]Spahr, H. R. and Wolf, D. F., "Theoretical Analysis of Wake-Induced Parachute Collapse," AIAA-81-1922, 1981.